PCCP

PAPER

View Article Online
View Journal | View Issue

Cite this: *Phys. Chem. Chem. Phys.*, 2025, **27**, 3988

First principles investigation of electron mobility enhancement of β-Ga_2O_3 doped with indium†

Leng Zhang,*[ab] Jiajian Huang,[b] Yuhao Shen,[a] Fei Liu,[b] Pengzhan Zhang,[b] Danbei Wang,[b] Kongping Wu[b] and Yaowei Wei[c]

Received 6th November 2024,
Accepted 2nd January 2025

DOI: 10.1039/d4cp04220d

rsc.li/pccp

β-Ga_2O_3 is one of the new-generation wide-bandgap semiconductor materials that has attracted much attention in recent years. However, the reported room-temperature electron mobility of β-Ga_2O_3 is much lower than GaN and SiC. Alloying Ga_2O_3 is expected to endow the material with superior carrier transport properties. Herein, we mainly investigate the electron mobility of pure Ga_2O_3, In-doped Ga_2O_3, and Al-doped Ga_2O_3 from first-principles considering acoustic deformation potential (ADP) scattering, polar optical phonon (POP) scattering and ionized impurity (IMP) scattering. The structure optimization, electronic band structure, and temperature-dependent and concentration-dependent electron mobility are investigated. The results show that the mobility of In–Ga_2O_3 is always the highest at 105–650 K, and POP scattering is the dominant factor limiting the electron mobility from 150–650 K. The mobility enhancement by In-doping is attributed to the smaller effective mass caused by the In 5s state despite its slightly increased electron–phonon coupling strength. The predicted electron mobilities for Ga_2O_3, Al–Ga_2O_3 and In–Ga_2O_3 at an electron concentration of 1.0×10^{17} cm^{-3} are 151.5 cm^2 V^{-1} s^{-1}, 137.8 cm^2 V^{-1} s^{-1} and 184.9 cm^2 V^{-1} s^{-1} at room temperature, respectively. This work provides an alternative route to enhance the electron mobility of Ga_2O_3 and guides in engineering their electronic transport properties for high-power electronics.

1. Introduction

Wide bandgap semiconductor materials, represented by gallium oxide (β-Ga_2O_3),[1] aluminum nitride (AlN),[2] and diamond,[3] have become the most promising materials for the new generation of semiconductors. Their high bandgap (>4.5 eV)[4] and high breakdown voltage (>1800 V)[5,6] significantly expand the depth and breadth of applications in electronic and optical devices. β-Ga_2O_3 has gained market favor due to its high-quality substrates and large-scale substrate production capabilities,[7] prompting in-depth exploration of performance optimization by the academic and commercial communities. In semiconductor devices, carrier transport properties are crucial as they determine the electrical performance. However, the reported room-temperature electron mobility of β-Ga_2O_3 remains below 200 cm^2 V^{-1} s^{-1},[8–12] which is 1 to 2 orders of magnitude lower than that of third-generation semiconductors like SiC, GaN, *etc.*,[13,14] hindering the efficiency and application range of Ga_2O_3 devices. Alloying Ga_2O_3 is expected to endow the material with superior carrier transport properties.

Existing research showed that doping could change the carrier mobility of semiconductors. Considering only acoustic phonon (rather than polar phonon) scattering, Zhang found that by doping with Cu and Sn, the electron mobility of Ga_2O_3 was enhanced significantly from 847 cm^2 V^{-1} s^{-1} to 12 409 cm^2 V^{-1} s^{-1} and 4217 cm^2 V^{-1} s^{-1},[15] respectively. Focusing on a simplified model based on deformation potential scattering, Yu found that the electron mobility of Ga_2O_3 was reduced from intrinsic 283.8 cm^2 V^{-1} s^{-1} to 207.7 cm^2 V^{-1} s^{-1}, 212.6 cm^2 V^{-1} s^{-1}, and 187.3 cm^2 V^{-1} s^{-1} by doping with Si, Ge and Sn.[16] Typically, the structure cells chosen for first principles calculation contain only several dozen atoms, in which even doping with one atom could result in heavy doping, leading to a band structure similar to that of metals or semimetals, when doping with elements that are not isoelectronic with Ga or O. In such cases, using a semiconductor model to calculate its electrical transport properties might not be accurate. Isoelectronic doping does not present this issue. Li calculated the impact of indium doping on the electrical properties of single-layer Ga_2O_3 metal–oxide–semiconductor field-effect transistors (MOSFETs) and discovered

[a] *National Laboratory of Solid State Microstructures and School of Physics, Nanjing University, Nanjing 210093, China. E-mail: zhangleng2018@jit.edu.cn*
[b] *School of Electronics and Information Engineering, Jinling Institute of Technology, Nanjing 211169, Jiangsu, P. R. China*
[c] *State Center for International Cooperation on Designer Low-Carbon & Environmental Materials (CDLCEM), School of Materials Science and Engineering, Zhengzhou University, Zhengzhou 450001, China*

† Electronic supplementary information (ESI) available. See DOI: https://doi.org/10.1039/d4cp04220d

that the on-current for high-performance and low-power achieved great improvement at In doping concentrations of 5% and 20%.[17] Using a chemical vapor deposition method, Tian found that In-doping enhanced the mobility of Ga_2O_3 nanobelts compared to pure Ga_2O_3, thereby improving the sensitivity and responsivity of Ga_2O_3 photodetectors,[18] consistent with Ji's experimental results.[19] Both theoretical and experimental studies have shown that the electron mobility of Ga_2O_3 could be improved by doping with indium. However, the scattering mechanisms in In-doped Ga_2O_3 have not been thoroughly studied yet. Moreover, literature has indicated that Al, which belongs to the same group as In, reduced the mobility when doped in Ga_2O_3.[20,21] It is worth noting that these two elements belonging to the same group contribute to completely different effects on Ga_2O_3. Therefore, this research aims to compare various properties of In-doped Ga_2O_3, pure Ga_2O_3 and Al-doped Ga_2O_3, and then to investigate the reasons behind In-doping enhancing the mobility of Ga_2O_3.

In this work, we emphasize the scattering mechanisms determining the electron mobility of Ga_2O_3, In–Ga_2O_3, and Al–Ga_2O_3, taking acoustic deformation potential (ADP) scattering, polar optical phonon (POP) scattering and ionized impurity (IMP) scattering fully into account. We computed the band structures and density of states for three different structures, as well as the necessary parameters for ADP, POP and IMP scattering. Additionally, we calculated the variations in ADP, POP, and IMP scattering between 105 and 650 K and their respective contributions to the total mobility. Lastly, we investigated the mobility enhancement mechanism of In-doped Ga_2O_3.

2. Computational methodology

There are two kinds of unequal Ga atoms in the lattice structure of β-Ga_2O_3, namely Ga_I with tetrahedral coordination and Ga_{II} with octahedral coordination, as shown in Fig. 1. We have calculated the doping formation energy of In and Al atoms substituting for Ga_I and Ga_{II}, from which we could conclude that Al atoms preferentially substitute for Ga_{II} atoms, while In atoms preferentially substitute for Ga_I atoms. All the DFT calculations were performed in the 1 × 2 × 1 monoclinic Ga_2O_3 supercell using the Vienna *ab initio* simulation package (VASP) code.[22,23] The generalized gradient approximation (GGA) involving the Perdew–Burke–Ernzerhof (PBE)[24] functional was employed to describe the exchange correlation potential. The plane wave cutoff energy was set to 400 eV for all calculations. For the optimization and other property calculations, 3 × 6 × 7 and 4 × 7 × 8 Monkhorst–Pack *k*-points sampling were applied. These calculations were performed with 1×10^{-8} eV per atom energy tolerance and 0.01 eV Å^{-1} force tolerance. To counteract the underestimation on the band gaps of GGA, and reproduce the correct band-structure of β-Ga_2O_3, the Heyd–Scuseria–Ernzerhof (HSE06) screened hybrid functional[25] was adopted to acquire the band structure as well, and the mixing parameter of 0.39 was set.

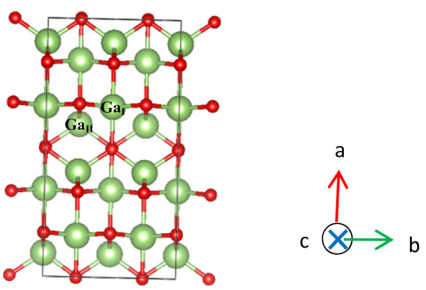

Fig. 1 Crystal structure of the Ga_2O_3 computational model. Green spheres represent cation antimony, and red spheres represent anion oxygen.

Based on the momentum relaxation time approximation, the electron mobility, μ_e, can be computed through the linearized Boltzmann transport equation (BTE),[26–29]

$$\mu_{e,\alpha\beta}^{MRTA} = \frac{e}{n_e \Omega} \sum_{n\varepsilon cb} \int \frac{d\mathbf{k}}{\Omega_{BZ}} \frac{\partial f_{n\mathbf{k}}^0}{\partial \varepsilon_{n\mathbf{k}}} v_{n\mathbf{k},\alpha} v_{n\mathbf{k},\beta} \tau_{n\mathbf{k}} \quad (1)$$

where α and β denote Cartesian coordinates, n_e is the electron concentration, Ω and Ω_{BZ} are the volumes of the unit cell and first Brillouin zone, respectively, $v_{n\mathbf{k},\alpha}$ and $v_{n\mathbf{k},\beta}$ are the group velocity weight of band index n and wave vector $\mathbf{k}$, "*cb*" stands for conduction bands, $f_{n\mathbf{k}}^0$ is the Fermi–Dirac distribution function, $\varepsilon_{n\mathbf{k}}$ is the electron energy, and $\tau_{n\mathbf{k}}$ is the electron lifetime. Based on the self-energy relaxation time approximation (SERTA),[27] the electron lifetimes can be obtained according to

$$\tau_{n\mathbf{k}}^{-1} = \sum_m \int \frac{d\mathbf{q}}{\Omega_{BZ}} \tau_{n\mathbf{k}\to m\mathbf{k}+\mathbf{q}}^{-1} \quad (2)$$

where $\tau_{n\mathbf{k}\to m\mathbf{k}+\mathbf{q}}^{-1}$ is the scattering rate of the transition from state $|n\mathbf{k}\rangle$ to state $|m\mathbf{k}+\mathbf{q}\rangle$. Two classes of scattering are implemented in the work: (i) inelastic scattering which occurs *via* emission or absorption of a phonon and (ii) perfectly elastic scattering in which no energy is gained or lost. In the case of inelastic scattering, the partial decay rate can be written as[30,31]

$$\tau_{n\mathbf{k}\to m\mathbf{k}+\mathbf{q}}^{-1} = \frac{2\pi}{\hbar} |g_{nm}(\mathbf{k},\mathbf{q})|^2 \times \left[\left(n_\mathbf{q} + 1 - f_{m\mathbf{k}+\mathbf{q}}^0 \right) \delta \left(\Delta\varepsilon_{\mathbf{k},\mathbf{q}}^{nm} - \hbar\omega_\mathbf{q} \right) + \left(n_\mathbf{q} + f_{m\mathbf{k}+\mathbf{q}}^0 \right) \delta \left(\Delta\varepsilon_{\mathbf{k},\mathbf{q}}^{nm} + \hbar\omega_\mathbf{q} \right) \right] \quad (3)$$

where $\hbar$ is the reduced Planck constant, $n_\mathbf{q}$ is the Bose–Einstein occupation, δ is the Dirac delta function, $\Delta\varepsilon_{\mathbf{k},\mathbf{q}}^{nm} = \varepsilon_{n\mathbf{k}} - \varepsilon_{m\mathbf{k}+\mathbf{q}}$. $|g_{nm}(\mathbf{k},\mathbf{q})|^2$ represents the matrix element of the interaction, which measures the probability amplitude of the transition from an initial state $n\mathbf{k}$ to final state $m\mathbf{k}+\mathbf{q}$ *via* a phonon with wave vector $\mathbf{q}$ and frequency $\omega_\mathbf{q}$. The $-\hbar\omega_\mathbf{q}$ and $+\hbar\omega_\mathbf{q}$ terms correspond to scattering by emission and absorption of a phonon, respectively. The scattering mechanism of POP belongs to inelastic scattering.[32]

For elastic scattering, the partial decay rate can be written as

$$\tau_{n\mathbf{k}\to m\mathbf{k}+\mathbf{q}}^{-1} = \frac{2\pi}{\hbar} |g_{nm}(\mathbf{k},\mathbf{q})|^2 \delta \left(\Delta\varepsilon_{\mathbf{k},\mathbf{q}}^{nm} \right) \quad (4)$$

The scattering mechanisms of IMP[33,34] and ADP[35–38] belong to elastic scattering. The matrix elements for ADP, IMP and POP are calculated, respectively. Before the total mobility can be obtained, the basic parameters are calculated firstly. These

include the ADP matrix parameters of the fully anisotropic acoustic deformation potential and elastic constants, POP matrix parameters including static (ε_s), high-frequency (ε_∞) dielectric constants and effective phonon frequency (ω_{po}), *etc.* Through Fourier interpolation in the first Brillouin zone to compute electron mobility by AMSET,[29] we can accurately evaluate the contribution of individual scattering mechanisms on a much-denser mesh of dimensions 13 × 25 × 27 after convergence tests.

3. Results and discussion

3.1. Electronic band structure

The lattice parameters of Ga_2O_3, Al–Ga_2O_3 and In–Ga_2O_3 are listed in Table 1. The calculated Ga_2O_3 lattice parameter results are in good agreement with the experimental data[39] (deviation less than 1.8%) and previous calculations,[40] demonstrating reliability of the employed theoretical methodology. Al–Ga_2O_3 has a slightly smaller lattice parameter, while In–Ga_2O_3 has a slightly larger lattice parameter, as Al atoms are smaller than Ga atoms while In atoms are larger than Ga atoms.

To explore the differences in energy band, electronic occupancy states, and effective electron mass between pure Ga_2O_3 and doped Ga_2O_3, we performed calculations of the band structure, total density of states (TDOS), and partial density of states (PDOS). Fig. 2(a)–(c) present the electronic band structures of Ga_2O_3, Al–Ga_2O_3 and In–Ga_2O_3 with a Brillouin zone path of G–F–Q–Z–G calculated using PBE (orange lines) and HSE (blue lines), respectively. This reveals that the electronic band structures predicted using PBE and HSE demonstrate the same dispersion shape, except for the bandgap values, which means that they have the equivalent effective mass closely related to the curvature of the band at the high symmetry point. The band gap of Ga_2O_3 (Fig. 2a) obtained using HSE and PBE is 4.91 and 2.05 eV respectively. The gap between the bandgap calculated by HSE and the experimental results of 4.86 eV[41] is very small. For Al–Ga_2O_3 (Fig. 2b), the band gap is 5.05 and 2.18 eV, respectively, while for In–Ga_2O_3 (Fig. 2c), the band gap is 4.77 and 1.93 eV, respectively. As HSE requires heavy computational resources, PBE is chosen to predict the carrier transport properties of these three Ga_2O_3 structures.

Table 1 Lattice constants of β-Ga_2O_3 compared with literature data

Lattice constant	*A*	*b*	*c*	*β*
Ga_2O_3-expt.[39]	12.23	3.04	5.80	103.7
Ga_2O_3-theory[40]	12.45	3.08	5.87	103.7
Ga_2O_3	12.32	3.07	5.70	103.69
Al–Ga_2O_3	12.30	3.07	5.68	103.64
In–Ga_2O_3	12.40	3.10	5.73	103.61

In this study, we only focus on the electron mobility. From the band diagram, it can be seen that the conduction band minimum (CBM) is located at the gamma point. The electron effective mass (m_c^*) is defined as:

$$\left(\frac{1}{m_c^*}\right)_{ij} = \frac{1}{\hbar^2}\frac{\partial^2 E_n\left(\vec{k}\right)}{\partial k_i \partial k_j}, \quad i,j = x,y,z \tag{5}$$

where x, y, and z are the directions in the reciprocal space $(2\pi/a)$, $E_n(\vec{k})$ is the dispersion relationship for the n-th electronic band. Using the effective mass calculator (EMC)[42] and finite difference method, we have calculated the effective mass at CBM, as shown in Table 2. The effective masses of pure Ga_2O_3 along x, y, and z are 0.22, 0.23, and 0.21, which are close to the values reported in the literature of 0.22, 0.22, and 0.21.[40] The electron effective mass distributions reveal that the electron effective mass m_c^* is basically isotropic, consistent with the subsequent mobility calculations. The effective masses of Al–Ga_2O_3 are 0.24, 0.24, and 0.23, slightly higher than pure Ga_2O_3, which is unfavorable for carrier transport; meanwhile the effective masses of In–Ga_2O_3 are 0.21, 0.22, and 0.21, slightly lower than pure Ga_2O_3, which is beneficial for carrier transport.

The total density of states (TDOS) curves for pure Ga_2O_3, Al–Ga_2O_3, and In–Ga_2O_3 are similar, as shown in Fig. 3. Near the valence band maximum (VBM), the states are mainly contributed by O 2p and Ga 3p states. The O 2p states are localized below VBM, leading to a flat valence band, bringing about large hole effective mass. The DOS near the CBM is very low, resulting in a steep conduction band, meaning Ga_2O_3 has small electron effective mass. Al 3s and Al 3p states have minimal contribution to CBM as shown in Fig. 3(b) and (d). In contrast, In–Ga_2O_3 shows slightly higher In 5s states near the CBM (3.5–5 eV), resulting in a higher TDOS, as shown in Fig. 3(c) and (e). However, in the region that determines the electron effective mass at the CBM (1.93–2.05 eV for In–Ga_2O_3, 2.06–2.15 eV for Ga_2O_3, circled in red), the TDOS of In–Ga_2O_3 is

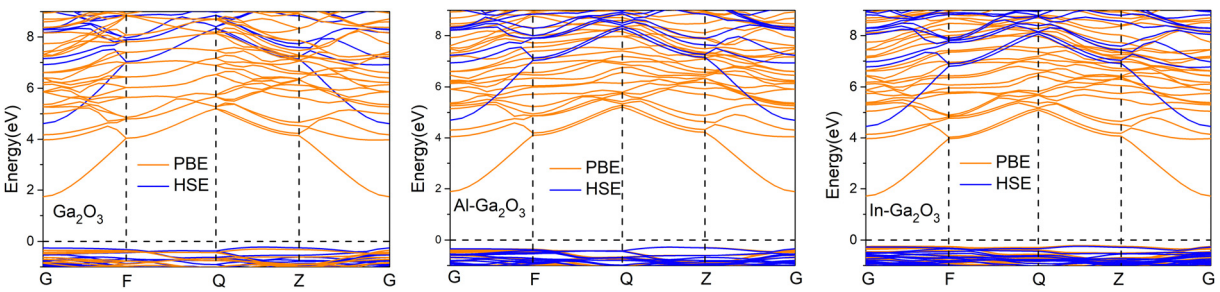

Fig. 2 Electronic band structures of pure Ga_2O_3, Al–Ga_2O_3, and In–Ga_2O_3 calculated using PBE (orange lines) and HSE (blue lines) functionals.

Table 2 Electron effective mass of Ga_2O_3, Al–Ga_2O_3 and In–Ga_2O_3 compared with literature data

	Electron effective mass (m_c^*/m_0)		
Structure	m_{xx}^*	m_{yy}^*	m_{zz}^*
Ga_2O_3[40]	0.22	0.22	0.21
Ga_2O_3	0.22	0.23	0.21
Al–Ga_2O_3	0.24	0.24	0.23
In–Ga_2O_3	0.21	0.22	0.21

the lowest caused main by the In 5s state, with less localization and a steeper CBM, resulting in a lower electron effective mass. The detailed TDOS of Ga_2O_3 and In–Ga_2O_3 near the CBM is shown in Table S1 (ESI†).

3.2. Electrical transport properties caused by ADP

Based on the electronic band structure, the scattering rate from ADP, POP, and IMP and the electron mobility could be calculated. Piezoelectric scattering was not considered as its proportion is very small. The electron mobility is calculated at moderate electron concentrations (1×10^{17} cm^{-3}). The methodology is introduced firstly for computing the transport properties, which enable us to discuss various factors influencing the electron mobility.

The ADP matrix element is given by[29]

$$g_{nm}^{\mathrm{ad}}(\mathbf{k},\mathbf{q}) = \sqrt{k_{\mathrm{B}}T}\sum_{\mathbf{G}\neq-\mathbf{q}}\left[\frac{\tilde{\mathbf{D}}_{nk}:\hat{\mathbf{S}}_l}{c_l\sqrt{\rho}}+\frac{\tilde{\mathbf{D}}_{nk}:\hat{\mathbf{S}}_{t1}}{c_{t1}\sqrt{\rho}}+\frac{\tilde{\mathbf{D}}_{nk}:\hat{\mathbf{S}}_{t2}}{c_{t2}\sqrt{\rho}}\right] \times\left\langle m\mathbf{k}+\mathbf{q}\left|e^{i(\mathbf{q}+\mathbf{G})\cdot\mathbf{r}}\right|n\mathbf{k}\right\rangle \quad (6)$$

where $\tilde{\mathbf{D}}_{\mathrm{nK}}$ is a deformation potential tensor that describes how the electronic states respond to lattice vibrations, $\hat{\mathbf{S}}_{\mathrm{l}}$, $\hat{\mathbf{S}}_{\mathrm{t1}}$ and $\hat{\mathbf{S}}_{\mathrm{t2}}$ represent the unit polarization vectors for the longitudinal acoustic mode (l) and two transverse acoustic modes ($t1$, and $t2$), respectively, and ρ represents the density of the material. The amplitude of the strain at any temperature T can be obtained from the potential energy of the acoustic phonon as $\sqrt{k_{\mathrm{B}}T/\rho c^2}$, where k_{B} is the Boltzmann constant. $\langle m\mathbf{k}+\mathbf{q}|e^{i(\mathbf{q}+\mathbf{G})\cdot\mathbf{r}}|n\mathbf{k}\rangle$ is the overlap integral between state $|n\mathbf{k}\rangle$ and state $|m\mathbf{k}+\mathbf{q}\rangle$, where the factor $e^{i(\mathbf{q}+\mathbf{G})\cdot\mathbf{r}}$ accounts for the phase factor associated with the phonon wavevector and reciprocal lattice vector.

The elastic constants (C) of pure Ga_2O_3 calculated in this study are 288.4 GPa, 412.6 GPa, and 401.7 GPa, slightly higher than the experimental values[43], as shown in Table 3. The deformation potential (D_{A}) and elastic constants of In–Ga_2O_3 are the smallest, while those of Al–Ga_2O_3 are the largest, with pure Ga_2O_3 falling in the middle. The value of D_{A}/C of In–Ga_2O_3 is the smallest, while in Al–Ga_2O_3 it is the largest. According to formula (6), g_{nm}^{ad} is proportional to D_{A}/C, indicating that In–Ga_2O_3 might have the smallest g_{nm}^{ad}. Detailed matrix of elastic constants and deformation potential are listed in the ESI.†

Fig. 4a shows the temperature-dependent anisotropic mobility caused by only ADP scattering. The calculated mobilities differ by about 30% for the different directions, equivalent to the values observed in ref. 44. Besides, the mobility caused by ADP decreases with increasing temperature. According to formula (6), the scattering caused by deformation potential is positively correlated with temperature; as the temperature rises, deformation potential scattering increases, leading to a decrease in mobility. Fig. 4b shows the isotropically averaged mobility variation of Ga_2O_3, Al–Ga_2O_3, and In–Ga_2O_3 with temperature. The mobility of In–Ga_2O_3 is the highest when only ADP scattering is considered.

3.3. Electrical transport properties caused by POP

The POP differential scattering rate is given by:

$$g_{nm}^{\mathrm{po}}(\mathbf{k},\mathbf{q}) = \left[\frac{\hbar\omega_{\mathrm{po}}}{2}\right]^{\frac{1}{2}}\sum_{\mathbf{G}\neq-\mathbf{q}}\left(\frac{1}{\hat{\mathbf{n}}\cdot\boldsymbol{\varepsilon}_\infty\cdot\hat{\mathbf{n}}}-\frac{1}{\hat{\mathbf{n}}\cdot\boldsymbol{\varepsilon}_{\mathrm{s}}\cdot\hat{\mathbf{n}}}\right)^{\frac{1}{2}} \times\frac{\langle m\mathbf{k}+\mathbf{q}|e^{i(\mathbf{q}+\mathbf{G})\cdot\mathbf{r}}|n\mathbf{k}\rangle}{|\mathbf{q}+\mathbf{G}|} \quad (7)$$

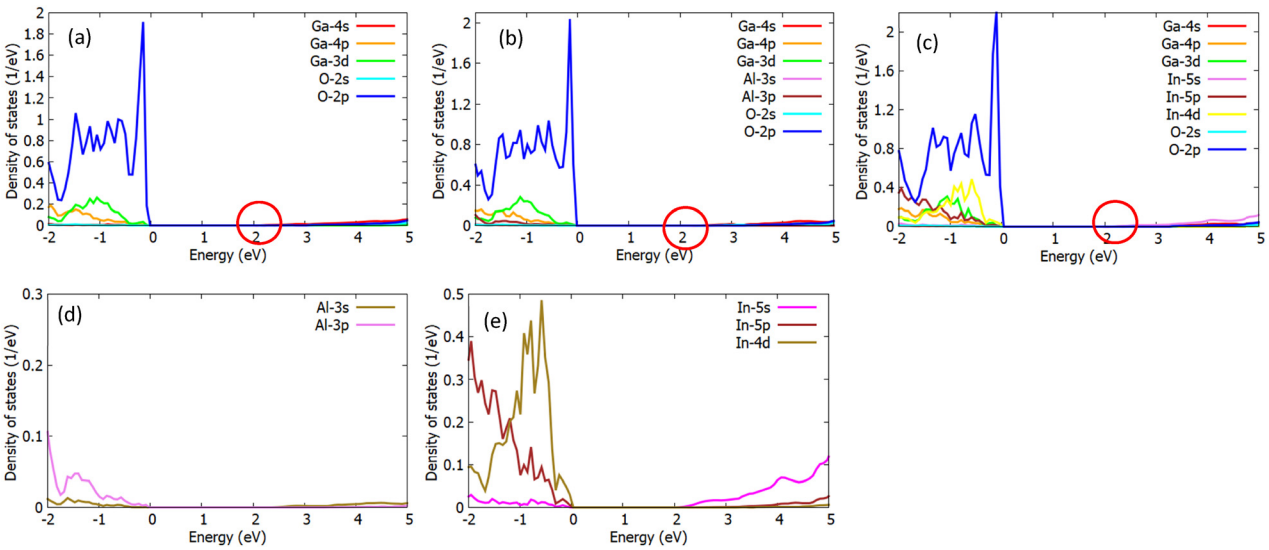

Fig. 3 TDOS of pure Ga_2O_3 (a), Al–Ga_2O_3 (b), and In–Ga_2O_3 (c); PDOS of Al in Al–Ga_2O_3 (d) and PDOS of In in In–Ga_2O_3 (e).

Table 3 Elastic constants and deformation potential of Ga_2O_3, Al–Ga_2O_3 and In–Ga_2O_3 compared with literature data

	C (GPa)			D_A (eV)		
	A	b	c	a	b	c
Ga_2O_3-expt[43]	242.8	343.8	347.4	—	—	—
Ga_2O_3	288.4	412.6	401.7	3.15	2.16	3.27
Al–Ga_2O_3	295.8	419.0	406.5	3.29	2.36	3.30
In–Ga_2O_3	281.8	403.9	385.2	2.88	2.17	2.93

where $\hbar\omega_{po}$ represents the frequency of the polar optical phonon mode, $\hat{\mathbf{n}}$ is a unit vector describing the direction of the phonon wavevector, while ε_∞ and ε_s are the high-frequency and static dielectric tensors of the material, respectively. The expression $\left(\frac{1}{\hat{\mathbf{n}}\cdot\varepsilon_\infty\cdot\hat{\mathbf{n}}}-\frac{1}{\hat{\mathbf{n}}\cdot\varepsilon_s\cdot\hat{\mathbf{n}}}\right)^{\frac{1}{2}}$ characterizes the difference in dielectric screening between high and low frequencies, influencing the strength of the long-range Coulomb interactions between electrons and phonons in polar materials.

In polar semiconductors, the charge carriers and the surrounding lattice deformation form a so-called polaron,[45] which determines the nature of carrier transport. Polarons can be classified into small and large ones based on the strength of electron phonon coupling. The lattice deformation in a large polaron is usually moderate and spreads over multiple unit cells, resulting in a larger mobility. The electron–phonon interaction is usually dominated by the coupling of charge carriers to the longitudinal optical phonons, which can be described within the Fröhlich model.[46] The coupling strength between electrons and polar optical phonons is quantified using the Fröhlich coupling constants[32,47]

$$\alpha=\frac{1}{2}\frac{1}{4\pi\varepsilon_0}\left(\frac{1}{\varepsilon_\infty}-\frac{1}{\varepsilon_s}\right)\frac{e^2}{\hbar\omega_{po}}\sqrt{\frac{2m_c^*\omega}{\hbar}} \quad (8)$$

where m_c^* is the CBM electron effective mass, and ε_0 is the vacuum permittivity. The above relevant material parameters of Ga_2O_3 are listed in Tables 2 and 5. The calculated α (shown in Table 4) shows the averaged value of 1.16, 1.25 and 1.17 for Ga_2O_3, Al–Ga_2O_3 and In–Ga_2O_3, which falls in the intermediate electron–phonon coupling regime (defined as $0.5 \le \alpha \le 6$). The magnitudes of α for Ga_2O_3 and In–Ga_2O_3 are quite close, suggesting similar electron–phonon interaction strengths. We further estimate the size of polarons in Ga_2O_3, Al–Ga_2O_3 and In–Ga_2O_3, by the Schultz polaron radius (r_f).[47] The large values of electron polaron radius (which extend over multiple structural units) indicate that the polarons are delocalized in these Ga_2O_3. Al–Ga_2O_3 has the smallest Schultz Polaron radius while Ga_2O_3 has the largest one, suggesting that the Fröhlich coupling strength of In–Ga_2O_3 is slightly larger than Ga_2O_3, and smaller than that of Al–Ga_2O_3.

$g_{nm}^{po}(k, q)$ is proportional to the frequency of the polar optical phonon mode, ω_{po}, and inversely proportional to the electronic high-frequency dielectric constant, ε_∞. As ε_∞ is much smaller than ε_s, the value of $\frac{1}{\hat{\mathbf{n}}\cdot\varepsilon_\infty\cdot\hat{\mathbf{n}}}-\frac{1}{\hat{\mathbf{n}}\cdot\varepsilon_s\cdot\hat{\mathbf{n}}}$ is almost equal to $\frac{1}{\hat{\mathbf{n}}\cdot\varepsilon_\infty\cdot\hat{\mathbf{n}}}$.

For purposes of the screening, we assume that the high-frequency dielectric constant is isotropic. Indeed, our DFPT calculations (see Table 5) show that the high-frequency part of the dielectric tensor is nearly isotropic, with values ranging between 3.98 and 4.10 depending on the direction, close to the theoretical value.[11,12] In contrast, the static dielectric tensor (ε_s) shows a stronger directional dependence, which is attributed to the anisotropic ionic contributions to the dielectric tensor in the monoclinic lattice. An averaged value of the computed ε_∞ (4.05) is used for calculating $g_{nm}^{po}(k, q)$ of Ga_2O_3. This value is close to the experimental value of ε_∞ = 3.60.[48] Besides, it is obvious that the ε_∞ of In–Ga_2O_3 is the largest, and the ω_{po} of In–Ga_2O_3 is the smallest, indicating g_{nm}^{po} of In–Ga_2O_3 might be the smallest among these three structures according to formula (7).

We further analyze the individual contribution of POP scattering, as shown in Fig. 5. The mobility of Ga_2O_3, Al–Ga_2O_3, and In–Ga_2O_3 exhibits similar variation curves with temperature, in which the mobility of In–Ga_2O_3 by POP individual scattering is always the highest. μ_{POP} reduces monotonically as the temperature increases. Since as temperature further increases, more polar optical phonons are excited which can

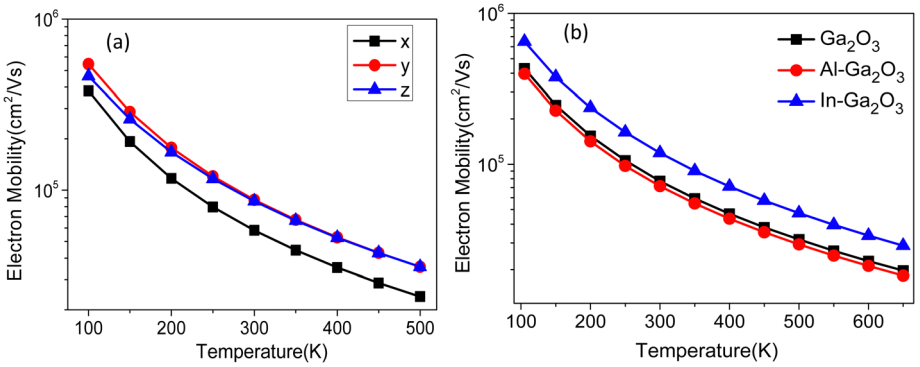

Fig. 4 Temperature-dependent electron mobility of Ga_2O_3 along *x*, *y*, and *z* directions (a) and the isotropically averaged mobility variation of Ga_2O_3, Al–Ga_2O_3 and In–Ga_2O_3 (b) when only ADP scattering is considered.

Table 4 Calculated Fröhlich parameter (α) and Schultz polaron radius (r_f) for electrons in Ga_2O_3, Al–Ga_2O_3, and In–Ga_2O_3 at T = 300 K

	α			r_f (Å)		
	Ga_2O_3	Al–Ga_2O_3	In–Ga_2O_3	Ga_2O_3	Al–Ga_2O_3	In–Ga_2O_3
Average	1.16	1.25	1.17	145.8	138.1	142.3

induce a macroscopic electric field, thus strengthening the electron–phonon coupling.

3.4. Electrical transport properties caused by IMP

The ionized impurity matrix element is given by

$$g_{nm}^{ii}(\mathbf{k},\mathbf{q}) = \sum_{\mathbf{G}\neq-\mathbf{q}} \frac{n_{ii}^{1/2} Ze}{\hat{\mathbf{n}}\cdot\boldsymbol{\varepsilon}_s\cdot\hat{\mathbf{n}}} \frac{\langle m\mathbf{k}+\mathbf{q}|e^{i(\mathbf{q}+\mathbf{G})\cdot r}|n\mathbf{k}\rangle}{|\mathbf{q}+\mathbf{G}|^2+\beta^2} \quad (9)$$

where n_{ii} is the ionized impurity density, representing the concentration of the electron that contributes to the interaction. Ze is the charge of the ionized impurity, where Z is the atomic number of the impurity (or the number of charges), and e is the elementary charge. The factor $\hat{\mathbf{n}}\cdot\varepsilon_s\cdot\hat{\mathbf{n}}$ modulates the strength of the Coulomb interaction due to screening effects. The denominator $|\mathbf{q}+\mathbf{G}|^2+\beta^2$ accounts for the momentum transfer $\mathbf{q}+\mathbf{G}$ during scattering, with β representing a screening length parameter that modulates the range of the interaction.

As shown in Fig. 6a, the mobility due to IMP slightly increases with rising temperature because, as the temperature increases, the kinetic energy of electrons increases, causing them to move faster and spend less time near recombination centers, thereby reducing the probability of scattering. Besides, our research has shown that the mobility of In–Ga_2O_3 is always higher than that of pure Ga_2O_3 and Al–Ga_2O_3. This might be partly attributed to the larger ε_s of In–Ga_2O_3.

The electron concentration is varied from 10^{13} cm^{-3} to 10^{18} cm^{-3} to explore the concentration dependent electron mobility of Ga_2O_3, Al–Ga_2O_3 and In–Ga_2O_3, respectively, as shown in Fig. 6b. With electron concentration increasing from 10^{13} to 10^{16} cm^{-3}, the electron mobility of In–Ga_2O_3 slightly drops from 228.9 cm^2 V^{-1} s^{-1} to 211.7 cm^2 V^{-1} s^{-1} at 300 K, respectively, which indicates the electron mobility of In–Ga_2O_3 remains essentially stable. After that, a further increase in electron concentration (from 10^{16} to 10^{18} cm^{-3}) rapidly deteriorates electron mobility, from 211.7 cm^2 V^{-1} s^{-1} to 138.4 cm^2 V^{-1} s^{-1} at 300 K. This is caused by the strong scattering of excessive carrier concentration with electrons and phonons. According to formula (9), the scattering intensity is positively correlated with impurity concentration n_{ii}: the higher the impurity (electron) concentration, the greater the electron scattering intensity, which hinders movement and decreases mobility.

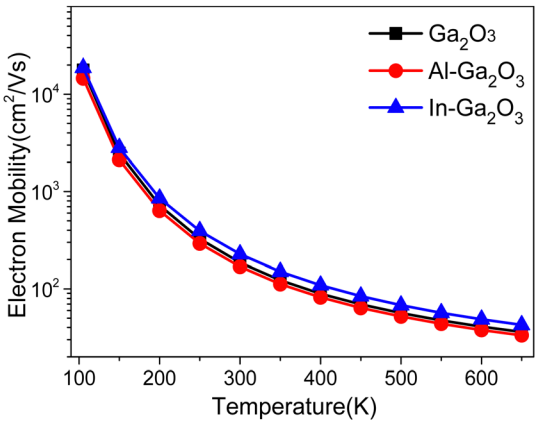

Fig. 5 Temperature-dependent electron mobility of Ga_2O_3, Al-doped Ga_2O_3 and In-doped Ga_2O_3, where only POP scattering is considered.

Based on Fig. 4b, 5 and 6a, in the temperature range of 105–150 K, μ_{IMP} is the lowest, indicating IMP scattering dominates the electron transport. In the temperature range of 150–650 K, μ_{ADP} and μ_{IMP} are much higher than μ_{POP}, indicating that POP scattering dominates the carrier transport of these three Ga_2O_3. Fig. 7 shows the effect of temperature on overall mobility, considering ADP, IMP, and POP together. Following Matthiessen's rule,[50] the total mobility μ_{total} is determined from $\mu_{total}^{-1} = \mu_{ADP}^{-1} + \mu_{IMP}^{-1} + \mu_{POP}^{-1}$. The total mobility is primarily determined by the smallest partial mobility. Overall, ADP has little effect on the total electron mobility. At low temperatures, impurity scattering significantly impacts the total electron mobility; as the temperature increases, optical phonon scattering gradually becomes the dominant scattering mechanism. The magenta curve in Fig. 7 shows the experimentally measured Hall mobility of pure Ga_2O_3,[9] while the black curve represents the mobility of pure Ga_2O_3 calculated in this study. The high degree of overlap between these two curves indicates the reliability of the calculation method employed in this research. The overall mobility of In–Ga_2O_3 (blue curve) is the highest from 105 to 650 K, and the electron mobilities of Ga_2O_3, Al–Ga_2O_3 and In–Ga_2O_3 are 151.5 cm^2 V^{-1} s^{-1}, 137.8 cm^2 V^{-1} s^{-1} and 184.9 cm^2 V^{-1} s^{-1} at 300 K. Since the effective mass of In–Ga_2O_3 is smaller than that of Ga_2O_3 and Al–Ga_2O_3, it still possesses higher mobility despite its slightly larger electron–phonon coupling strength.

Table 5 The parameters of POP scattering of β-Ga_2O_3 compared with literature data

	ε_∞				ε_s				
Materials	*a*	*b*	*c*	Average	*a*	*b*	*c*	Average	ω_{po} (THz)
Ga_2O_3[11]	4.07	4.14	4.19	4.13	10.99	10.50	13.91	11.80	12.08, 8.46–11.60[49]
Ga_2O_3[12]	4.02	4.03	4.15	4.10	11.88	9.22	12.61	11.24	
Ga_2O_3	3.98	4.06	4.10	4.05	10.20	9.55	13.71	11.15	13.12
Al–Ga_2O_3	3.91	3.99	4.00	3.97	10.09	9.48	13.04	10.87	12.75
In–Ga_2O_3	4.01	4.10	4.12	4.08	10.32	9.49	13.90	11.24	12.71

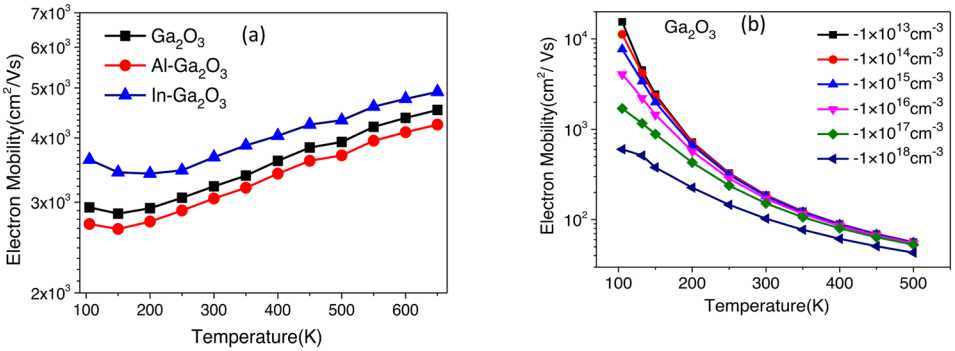

Fig. 6 Temperature-dependent electron mobility of Ga_2O_3 at electron concentrations (1×10^{17} cm^{-3}) where only IMP scattering is considered (a). Temperature-dependent electron mobility of Ga_2O_3 at various electron concentrations where ADP, IMP and POP scattering are considered together (b).

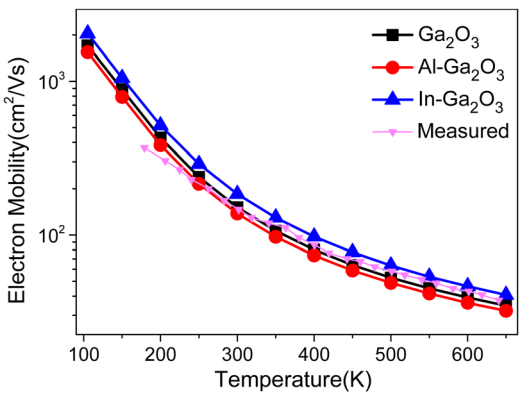

Fig. 7 Temperature-dependent electron mobility of Ga_2O_3, Al-doped Ga_2O_3 and In-doped Ga_2O_3, where ADP, IMP and POP scattering are considered together.

4. Conclusions

To summarize, we have investigated the temperature-dependent electron mobility of Ga_2O_3, Al–Ga_2O_3 and In–Ga_2O_3 from first-principles by fully considering the scattering mechanisms of ADP, IMP, and POP. The results show that POP scattering is the dominant factor limiting the electron mobility of Ga_2O_3, Al–Ga_2O_3 and In–Ga_2O_3 between 150 and 650 K. Combining these three scattering mechanisms, the electron mobilities of Ga_2O_3, Al–Ga_2O_3 and In–Ga_2O_3 are 151.5 $cm^2\ V^{-1}\ s^{-1}$, 137.8 $cm^2\ V^{-1}\ s^{-1}$ and 184.9 $cm^2\ V^{-1}\ s^{-1}$ at 300 K. Furthermore, as temperature increases, the electron mobility of three Ga_2O_3 reduces due to more excited optical phonons, thus enhancing the electron–phonon coupling. With electron concentration increasing, the electron mobility of three Ga_2O_3 reduces due to more scattering probabilities. The electron mobility of In–Ga_2O_3 is the highest among these three structures for the decreased effective mass caused by the In 5s state. This work offers an alternative method to boost the electron mobility of Ga_2O_3 and serves as a guide for engineering the electronic transport properties tailored for high-power electronic applications.

Author contributions

L. Z.: conceptualization, software, writing – original draft. J. H.: validation. Y. S.: writing – review & editing. F. L. and P. Z: formal analysis, visualization. D. W.: visualization. K. W.: writing – review & editing, supervision. Y. W.: writing – original draft, supervision.

Data availability

The data that support the findings of this study are available within the article and the ESI.†

Conflicts of interest

There are no conflicts to declare.

Acknowledgements

This work is financially supported by the National Natural Science Foundation of China (Grant No. 61904071), the QingLan Project of Jiangsu Provincial University of China and the Science Foundation of Jinling Institute of Technology (jit-rcyj-202001). We are thankful for the technology support from the National Supercomputer Center (TianHe-2) in Lvliang.

References

1 X. He, J. Hu and Z. Zhang, *et al.*, Study on the interface electronic properties of AlN(0001)/β-Ga_2O_3 (100), *Surf. Interfaces*, 2022, **28**, 101585.
2 N. Pant, W. Lee and N. Sanders, *et al.*, Increasing the mobility and power-electronics figure of merit of AlGaN with atomically thin AlN/GaN digital-alloy superlattices, *Appl. Phys. Lett.*, 2022, **121**(3), 032105.
3 C. J. H. Wort and R. S. Balmer, Diamond as an electronic material, *Mater. Today*, 2008, **11**, 22–28.

4 H. H. Tippins, Optical absorption and photoconductivity in the band edge of β-Ga_2O_3, *Phys. Rev.*, 1965, **140**(1A), A316–A319.
5 K. Wu, L. Zhang, F. Li, L. Sang, M. Liao, K. Tang, J. Ye and S. Gu, Enhancement of interfacial thermal conductance by introducing carbon vacancy at the Cu/diamond interface, *Carbon*, 2024, **223**, 119021.
6 M. Higashiwaki, K. Sasaki and A. Kuramata, *et al.*, Gallium oxide Ga_2O_3 metal-semiconductor field-effect transistors on single-crystal β-Ga_2O_3 substrates, *J. Appl. Phys. Lett.*, 2012, **100**(1), 013504.
7 Z. Galazka, R. Uecker and K. Lrmscher, *et al.*, Czochralski growth and characterization of β-Ga_2O_3 single crystalsJ, *Cryst. Res. Technol.*, 2010, **45**(12), 1229–1236.
8 Encarnación G. Villora, Kiyoshi Shimamura, Takekazu Ujiie and Kazuo Aoki, Electrical conductivity and lattice expansion of β-Ga_2O_3 below room temperature, *Appl. Phys. Lett.*, 2008, **92**, 202118.
9 N. Ma, N. Tanen, A. Verma, Z. Guo, T. Luo, H. (Grace) Xing and D. Jena, Intrinsic Electron Mobility Limits in -Ga_2O_3, *Appl. Phys. Lett.*, 2016, **109**, 212101.
10 Z. Zhang, Y. Wu, C. Lu and S. Ahmed, Electron mobility in β-Ga_2O_3: an ensemble Monte Carlo study, *Appl. Phys. A*, 2018, **124**, 637.
11 X. Duan, T. Wang, Z. Fu, L. Liu and J. Yang, Nontrivial role of polar optical phonons in limiting electron mobility of two-dimensional Ga_2O_3 from first-principles, *Phys. Chem. Chem. Phys.*, 2023, **25**, 10175–10183.
12 Y. Kang, K. Krishnaswamy, H. Peelaers and C. G. Van de Walle, Fundamental limits on the electron mobility of β-Ga_2O_3, *J. Phys.: Condens. Matter*, 2017, **29**, 234001.
13 F. Roccaforte, P. Fiorenza, G. Greco, R. L. Nigro, F. Giannazzo, F. lucolano and M. Saggio, Emerging trends in wide band gap semiconductors (SiC and GaN) technology for power devices, *Microelectro. Eng.*, 2018, **187–188**, 66–77.
14 B. K. Ridley, B. E. Foutz and L. F. Eastman, Mobility of electrons in bulk GaN and $Al_xGa_{1-x}N$/GaN heterostructures, *Phys. Rev. B: Condens. Matter Mater. Phys.*, 2000, **61**, 16862–16869.
15 C. Zhang, F. Liao, X. Liang, H. Gong, Q. Liu, L. Li, X. Qin, X. Huang and C. Huang, Electronic transport properties in metal doped beta-Ga_2O_3: A first principles study, *Phys. B*, 2019, **562**, 124–130.
16 M. Yu, B. Peng, K. Sun, J. Yu, L. Yuan, J. Hu, Y. Zhang and R. Jia, First principles investigation of photoelectric properties of Ga_2O_3 Doped with group IV elements (Si,Ge,Sn), *Mater. Today Commun.*, 2023, **34**, 105127.
17 P. Li, L. Dong, C. Li, B. Lu, C. Yang, B. Peng, W. Wang, Y. Miao and W. Liu, Indium doping-assisted monolayer Ga_2O_3 exfoliation for performance-enhanced MOSFETs, *Nanoscale*, 2023, **15**, 12105–12115.
18 W. Tian, C. Zhi, T. Zhai, S. Chen, X. Wang, M. Liao, D. Golberg and Y. Bando, In-doped Ga_2O_3 nanobelt based photodetector with high sensitivity and wide-range photoresponse, *J. Mater. Chem.*, 2012, **22**, 17984–17991.
19 L. Ji, X. Chen, X. Su, J. Wan, Z. Tu, H. Wu and C. Liu, Influence of indium doping on electrical performance of gallium oxide thin-film transistors, *Appl. Phys. Lett.*, 2023, **122**, 202105.
20 J. Rehm, T. Chou, S. B. Anooz, P. Seyidov, A. Fiedler, Z. Galazka and A. Popp, Perspectives on MOVPE-grown (100) β-Ga_2O_3 thin films and its Al-alloy for power electronics application, *Appl. Phys. Lett.*, 2022, **121**, 240503.
21 Z. Xi, N. Chen, J. Cai, C. Xu, S. Li and S. Zheng, Modulation of electronic structures and transport properties in 2D TM0.5Ga1.5O3 (TM = Al, Ga, In), *Phys. Lett. A*, 2024, **525**, 129914.
22 G. Kresse and J. Furthmüller, Efficient iterative schemes for ab initio total energy calculations using a plane-wave basis set, *Phys. Rev. B: Condens. Matter Mater. Phys.*, 1996, **54**, 11169.
23 G. Kresse and J. Furthmüller, Efficiency of ab-initio total energy calculations for metals and semiconductors using a plane-wave basis set, *Comput. Mater. Sci.*, 1996, **6**, 15.
24 J. P. Perdew, K. Burke and M. Ernzerhof, Generalized gradient approximation made simple, *Phys. Rev. Lett.*, 1996, **77**, 3865.
25 J. Heyd, G. E. Scuseria& and M. Ernzerhof, Hybrid functionals based on a screened Coulomb potential, *J. Chem. Phys.*, 2003, **118**, 8207.
26 S. Poncé, W. Li, S. Reichardt and F. Giustino, First-principles calculations of charge carrier mobility and conductivity in bulk semiconductors and two-dimensional materials, *Rep. Prog. Phys.*, 2020, **83**, 036501.
27 S. Poncé, E. R. Margine and F. Giustino, Towards predictive many-body calculations of phonon-limited carrier mobilities in semiconductors, *Phys. Rev. B*, 2018, **97**, 121201.
28 W. Li, Electrical transport limited by electron-phonon coupling from Boltzmann transport equation: An ab initio study of Si, Al, and MoS_2, *Phys. Rev. B: Condens. Matter Mater. Phys.*, 2015, **92**, 075405.
29 A. M. Ganose, J. Park, A. Faghaninia, R. Woods-Robinson, K. A. Persson and A. Jain, Efficient calculation of carrier scattering rates from first principles, *Nat. Commun.*, 2021, **12**, 2222.
30 G. Grimvall, *The Electron-Phonon interaction in metals*, North-Holland, Amsterdam, 1981.
31 F. Giustino, M. L. Cohen and S. G. Louie, Electron-phonon interaction using Wannier functions, *Phys. Rev. B: Condens. Matter Mater. Phys.*, 2007, **76**, 165108.
32 H. Fröhlich, Electrons in lattice fields, *Adv. Phys.*, 1954, **3**, 325–361.
33 H. Brooks, Scattering by ionized impurities in semiconductors, *Phys. Rev.*, 1951, **83**, 879.
34 C. Herring and E. Vogt, Transport and deformation-potential theory for many-valley semiconductors with anisotropic scattering, *Phys. Rev.*, 1956, **101**, 944.
35 J. Bardeen and W. Shockley, Deformation potentials and mobilities in non-polar crystals, *Phys. Rev.*, 1950, **80**, 72.
36 F. S. Khan and P. B. Allen, Deformation potentials and electron-phonon scattering: Two new theorems, *Phys. Rev. B: Condens. Matter Mater. Phys.*, 1984, **29**, 3341.
37 E. Kartheuser and S. Rodriguez, Deformation potentials and the electron-phonon interaction in metals, *Phys. Rev. B: Condens. Matter Mater. Phys.*, 1986, **33**, 772.

38 R. Resta, Deformation-potential theorem in metals and in dielectrics, *Phys. Rev. B: Condens. Matter Mater. Phys.*, 1991, **44**, 11035.
39 S. Geller, Crystal Structure of β-Ga_2O_3, *J. Chem. Phys.*, 1960, **33**, 676–684.
40 Q. Fan, R. Zhao, W. Zhang, Y. Song, M. Sun and U. Schwingenschlögl, Low-energy Ga_2O_3 polymorphs with low electron effective masses, *Phys. Chem. Chem. Phys.*, 2022, **24**, 7045–7049.
41 S. J. Pearton, J. Yang, P. H. Cary, F. Ren, J. Kim, M. J. Tadjer and M. A. Mastro, A review of Ga_2O_3 materials, processing, and devices, *Appl. Phys. Lett.*, 2018, **5**, 011301.
42 Effective Mass Calculator for Semiconductors, Fonari A, Sutton C, **https://github.com/afonari/emc2013-3-18**.
43 K. Adachi, H. Ogi, N. Takeuchi, N. Nakamura, H. Watanabe, T. Ito and Y. Ozaki, Unusual elasticity of monoclinic β-Ga_2O_3, *J. Appl. Phys.*, 2018, **124**, 085102.
44 M. H. Wong, K. Sasak, A. Kuramata, S. Yamakoshi and M. Higashiwaki, Electron channel mobility in silicon-doped Ga2O3 MOSFETs with a resistive buffer layer, *Jpn. J. Appl. Phys.*, 2016, **55**, 1202B9.
45 D. Emin, *Polarons*, Cambridge University Press, 2013.
46 H. Fröhlich, Interaction of electrons with lattice vibrations, *Proc. Math. Phys. Eng.*, 1952, **215**, 291–298.
47 J. M. Frost, Calculating polaron mobility in halide perovskites, *Phys. Rev. B*, 2017, **96**, 195202.
48 G. Schmitz, P. Gassmann and R. Franchy, A combined scanning tunneling microscopy and electron energy loss spectroscopy study on the formation of thin, well-ordered β-Ga_2O_3 films on CoGa (001), *J. Appl. Phys.*, 1998, **83**, 2533–2538.
49 T. Onuma, S. Saito, K. Sasaki, K. Goto, T. Masui, T. Yamaguchi, T. Honda, A. Kuramata and M. Higashiwaki, Temperature-dependent exciton resonance energies and their correlation with IR-active optical phonon modes in β-Ga_2O_3 single crystals, *App. Phys. Lett.*, 2016, **108**, 101904.
50 B. R. Nag, *Electron Transport in Compound Semiconductors*, Springer Berlin Heidelberg, Berlin, Heidelberg, 1980, vol. 11.

